

Global Atmospheric Sensitivity to Tropical SST Anomalies throughout the Indo-Pacific Basin

JOSEPH J. BARSUGLI AND PRASHANT D. SARDESHMUKH

NOAA-CIRES Climate Diagnostics Center, Boulder, Colorado

(Manuscript received 27 November 2001, in final form 29 May 2002)

ABSTRACT

The sensitivity of the global atmospheric response to sea surface temperature (SST) anomalies throughout the tropical Indian and Pacific Ocean basins is investigated using the NCEP MRF9 general circulation model (GCM). Model responses in January are first determined for a uniform array of 42 localized SST anomaly patches over the domain. Results from the individual forcing experiments are then linearly combined using a statistically based smoothing procedure to produce sensitivity maps for many target quantities of interest, including the geopotential height response over the Pacific-North American (PNA) region and regional precipitation responses over North America, South America, Africa, Australia, and Indonesia.

Perhaps the most striking result from this analysis is that many important targets for seasonal forecasting, including the PNA response, are most sensitive to SST anomalies in the Niño-4 region (5°N–5°S, 150°W–160°E) of the central tropical Pacific, with lesser and sometimes opposite sensitivities to SST anomalies in the Niño-3 region (5°N–5°S, 90°–150°W) of the eastern tropical Pacific. However, certain important targets, such as Indonesian rainfall, are most sensitive to SST anomalies outside both the Niño-4 and -3 regions.

These results are also relevant in assessing atmospheric sensitivity to changes in tropical SSTs on decadal to centennial scales associated with natural as well as anthropogenic forcing. In this context it is interesting to note the surprising result that warm SST anomalies in one-third of the Indo-Pacific domain lead to a *decrease* of global mean precipitation.

1. Introduction

The field of seasonal forecasting has matured considerably in the past decade. Operational forecasting centers now use both empirical and numerical models to make skillful forecasts of temperature, precipitation, and geopotential heights one or more seasons in advance for many parts of the globe. The success of these models is due in large part to their ability to capture the global atmospheric response to tropical sea surface temperature anomalies that are associated with the El Niño–Southern Oscillation phenomenon (ENSO).

Maturity in the field has brought some unsettling realizations. After years of model development, a large portion of seasonal climate variability is still poorly predicted. In addition, very simple linear empirical models remain competitive in skill with comprehensive atmospheric general circulation models (Peng et al. 2000; Kumar et al. 1996), leading one to ask if one is nearing the limits of predictability. While the single best strategy for improving seasonal forecasts is not obvious, the question of the influence of non-ENSO related SST anomalies naturally arises as an important issue. Do

current models have the correct sensitivities to such SST anomalies? Do they result in a predictable atmospheric signal, or do they add to the unpredictable noise? A comprehensive and systematic understanding of the global atmospheric sensitivity to all tropical SST anomalies, not just those associated with ENSO, would help answer these questions. Knowing the general sensitivity to SSTs would also help in anticipating the response to SST forcing on decadal to centennial scales where SST patterns depart even more from the canonical ENSO pattern than on the seasonal to interannual timescales.

In this paper we investigate the sensitivity of the global atmosphere in January to SST anomalies throughout most of the tropical Indian and Pacific Ocean basins. To accomplish this we performed a large ensemble of simulations with an atmospheric general circulation model (GCM) using an array of localized SST anomaly patches spanning this region (Fig. 1a). Analysis of the responses to individual patches allows us to determine the locations where SST anomalies are most effective at forcing a given “target” response—such as precipitation or geopotential height in some remote locale. In section 5 of this paper we show maps of this sensitivity for several targets of meteorological interest worldwide. As we shall see, the Niño-4 region—a rectangular area on the equator straddling the dateline (5°N–5°S, 150°W–

Corresponding author address: Dr. Joseph Barsugli, CIRES, University of Colorado, Campus Box 449, Boulder, CO 80309-0449.
E-mail: jjb@cdc.noaa.gov

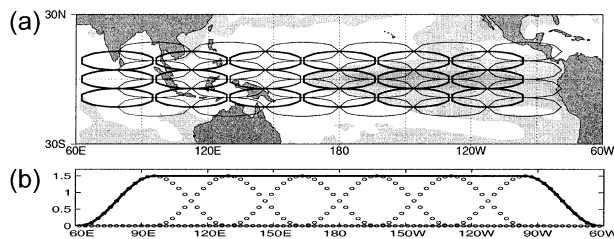


FIG. 1. (a) Grid of SST anomaly patches (contours) and standard deviation of Jan monthly mean SST (0.5 K, light shading; and 1.0 K, dark shading). The 0.75-K contour is shown for each anomaly patch. SST anomaly patches with central latitudes of 12.56° , 4.19° , -4.19° , and -12.56° (positive north) each have central longitudes of 264.375° , 230.625° , 196.875° , 163.125° , 129.375° , and 95.625° (positive east). Patches with central latitudes of 8.37° , 0.0° , and -8.37° each have central longitudes of 247.5° , 213.75° , 180.0° , 146.25° , 112.5° , and 78.75° . (b) Cross section in longitude through the peaks of the northernmost row of SST anomaly patches. Circles denote the model's Gaussian grid points. Solid line is the sum of these patches, illustrating that the individual patches add up to a "plateau."

160°E)—shows up repeatedly as the most effective region of SST forcing for many remote targets. Clearly this underscores the need to improve prediction of SST anomalies in Niño-4. Niño-4 is not the whole story, however. Our method can, and does, detect other sensitive areas of forcing. For example, precipitation in several regions such as the northwestern United States and Indonesia are most sensitive to SSTs outside of Niño-4.

The physical interpretation of the sensitivities we will show relies on understanding the basic chain of events leading from tropical SST anomalies to the global atmospheric response in this model. Ignoring many complexities, this chain of events can be described as follows. First the prescribed SST anomalies cause local changes in the low-level temperatures, winds, and humidity, usually leading to precipitation anomalies in the vicinity of the SST anomaly. These precipitation anomalies (mostly convective) are associated with deep latent heating and upper-level divergence anomalies that excite equatorial Rossby and Kelvin waves, spreading the influence throughout the Tropics. The resulting precipitation anomalies *throughout the Tropics* force extratropical Rossby waves, both directly via upper-level divergence and through the effect of the divergent wind on climatological vorticity gradients (Sardeshmukh and Hoskins 1988). These Rossby waves spread the influence globally, interacting with the climatological mean flow, orography, and transient eddies along the way.

Analysis of these runs involves several important technical issues arising mainly from the relatively small signal-to-noise ratio of the response to each SST patch. In essence, to increase the statistical significance of the features shown we have reduced the spatial resolution of the sensitivities by applying a statistically based smoother. The amount of smoothing depends on the signal-to-noise ratio of each target. In general the

smoothing is lighter for tropical targets and more severe for midlatitude targets. We address these issues in section 3 of this paper.

Our GCM runs may be formally viewed as determining the "Green's function" for the atmospheric response to tropical SST anomalies. The underlying assumption is that the seasonal (and longer-term) mean response to any large-scale SST pattern may be expressed as a linear combination of the responses to our localized SST patches. Borrowing a term from statistical physics, we call this "coarse-grain" linearity. Although the governing equations of the full GCM are nonlinear, quantities that have been averaged in space and time may be dominated by linear dynamics. We test this hypothesis by comparing combinations of the individual responses to separate GCM simulations with SST anomalies of larger scale. The evidence presented in section 4 supports coarse-grain linearity over large parts of the globe. To be sure, our Green's function approach only approximates the full GCM response. Still, it is a major conceptual simplification that enables one to anticipate the response to a much larger set of SST anomaly patterns than is possible through direct simulations.

The Green's function approach to the study of tropical-extratropical interactions goes back at least as far as Simmons et al. (1983). They applied a grid of localized vorticity forcing anomalies in a barotropic model (run at small, linear amplitudes) and plotted a map that qualitatively showed the sensitivity of the response to the forcing location. Branstator (1985) made the Green's function approach explicit when he applied single-grid-point forcing anomalies in a barotropic model linearized about the January basic state taken from a GCM. He also computed sensitivity maps for midlatitude targets, finding that atmospheric heating in the region around and north of Indonesia were particularly effective at forcing height anomalies over North America. Newman and Sardeshmukh (1998) have to date conducted the most comprehensive sensitivity analysis of this type with a linear barotropic model, with particular emphasis on how the most sensitive areas of forcing change with season.

In a baroclinic setting, several scientists have investigated the sensitivity of the midlatitude response to the location of tropical forcing without explicitly computing a Green's function. A notable early example is Simmons (1982). Building on this early work, Ting and Sardeshmukh (1993) investigated the linear baroclinic response of the atmosphere to localized heating anomalies at various longitudes on the equator. For the observed December–February (DJF) basic state they found that the midlatitude response was modal in character, dominated by a single spatial pattern. A nodal line in the forcing was found at 120°E longitude—that is, forcing slightly west or east of this nodal line resulted in responses of opposite sign over the Pacific–North American (PNA) region. However the structure of the modal response, as well as its sensitivity to forcing near 120°E , was quite

different when a basic state taken from the Geophysical Fluid Dynamics Laboratory (GFDL) GCM was considered. We will discuss these results later in comparison with sensitivities we find for the PNA pattern.

Although steady-state linear dynamical models provide a theoretical framework for the general analysis of sensitivities, they lack transient-eddy feedbacks and the physical processes that determine such important climate variables as precipitation and surface temperature. The linear models mentioned above require atmospheric heating anomalies to be specified, whereas a GCM can treat the SSTs themselves as inputs and allow the model's dynamics and physical parameterizations to determine the atmospheric heating.

The first two GCM experiments to investigate sensitivity to regional tropical SST anomalies yielded conflicting results. Palmer and Mansfield (1984) showed much stronger extratropical response to SST anomalies in the western Pacific than to those in the eastern Pacific. In fact they attributed much of the Northern Hemisphere 500-hPa height pattern in January 1977 to tropical SST anomalies west of 155°E longitude. Geisler et al. (1985) specified three nearly basin-scale SST anomalies in the central, eastern, and far-eastern Pacific. Their results showed a marked insensitivity of the January extratropical response to the position of the tropical forcing. However, both these studies were plagued by the problems inherent in GCM modeling of that era—crude physical parameterizations, questionable model climatologies, and inadequate sampling. A decade later, Ferranti et al. (1994) also investigated the DJF response to localized tropical SST anomalies, in this case over Indonesia and the Caribbean. The Indonesian SST anomaly had a strong downstream and poleward influence over the North Pacific, but the Caribbean anomalies had only a small influence over Europe.

The above studies were intended to give only a qualitative picture of sensitivity. Our project is rather more ambitious: to quantify atmospheric sensitivity to tropical SST anomalies throughout the Indo-Pacific domain with unprecedented spatial resolution and statistical sampling. This paper attempts to accomplish this for January conditions in one GCM. Some early results were presented in Barsugli et al. (1997).

2. Model and numerical experiment design

We use the National Centers for Environmental Prediction (NCEP) MRF9 atmospheric GCM (with T40 horizontal spectral truncation and 18 sigma-coordinate vertical levels) run in perpetual January conditions. We first performed a 70-month control run with climatological SST specified globally from which eight initial conditions were chosen for the experiments described below. The model and choice of initial conditions are described in more detail in appendix A. Kumar et al. (1996) and Sardeshmukh et al. (2000) document the realistic response of this model to observed SSTs, pro-

viding a justification for using this model to study seasonal climate anomalies.

Specification of localized SST anomalies is a critical element of our methodology. We choose a set of SST anomaly patches that covers most of the tropical Indian and Pacific Ocean basins (Fig. 1a). Each anomaly patch T_k , $k = 1, \dots, 42$, is a localized cosine hump of the form

$$T_k(\lambda, \phi) = B \cos^2\left(\frac{\pi}{2} \frac{\phi - \phi_k}{\phi_w}\right) \cos^2\left(\frac{\pi}{2} \frac{\lambda - \lambda_k}{\lambda_w}\right)$$

on the rectangle $\phi_k \pm \phi_w$, $\lambda_k \pm \lambda_w$ (where ϕ is latitude and λ is longitude), and zero elsewhere. The values of $T_k(\lambda, \phi)$ are specified on the Gaussian transform grid of the GCM. The half-width of the humps are chosen to be 12 grid points in longitude and 3 grid points in latitude, yielding $\lambda_w = 33.75^\circ$ and $\phi_w \approx 8.4^\circ$. The central points (λ_k, ϕ_k) , listed in Fig. 1, are arranged on a staggered grid. Note that this staggered grid is made up of two overlapping rectangular subgrids. In each subgrid, the space between the centers of the humps equals the half-width of the humps, so that adjacent patches add up to a uniform plateau (Fig. 1b).

Two sets of SST anomaly files were constructed: a warm anomaly set with amplitude $B = +1.5$ K, and a cold anomaly set with amplitude $B = -1.5$ K. The SST anomaly patches were added to the 1950–95 January climatological mean SST determined from the Smith et al. (1996) dataset, which consists of EOF reconstructed fields for the period 1950–81 and optimal interpolation analyses for 1982–95. The Smith et al. SST fields were also used in the Atmospheric Model Intercomparison Project (AMIP) style historical SST runs made with this GCM (Chen and Van den Dool 1997; Livezey et al. 1997) that are discussed in section 4c of this paper.

The SST anomaly size and amplitude were chosen based on inspection of a previous set of runs (the “Niño” experiments described in section 4b) so that the anomaly patches would be small enough to yield interesting structure in the sensitivity maps but large enough to give rise to a reasonable signal-to-noise ratio in the midlatitudes. An obvious question arises: Does a 1.5-K anomaly lead to a roughly linear precipitation response throughout the domain, even in regions such as the warm pool where the natural variability is smaller than 1.5 K? In section 4a we test this by comparing the local precipitation response for the warm and cold experiments separately.

An ensemble of eight 4-month runs was performed for each of the 42 “warm” SST anomaly patches, and again for each of the 42 “cold” SST anomaly patches. The climatological SST case was rerun for each initial condition, amounting to a total of 2720 months, or about 226 yr, of model simulation. Monthly mean output was saved.

3. Green's functions and sensitivity maps

The SST patch functions are localized in space, so we may think of the ensemble-mean response to an

individual patch as akin to a Green's function for forcing in that location. We can then construct the response to an arbitrary SST anomaly as the sum of the individual responses. Several technical issues arise when we attempt to do this, and we address these issues briefly in this section. For those who wish to skip the details, the essence of this section is that a robust estimation of the Green's function and the sensitivity maps is obtained by applying a statistically based smoother to the individual responses, trading off spatial resolution of the sensitivities for increased statistical significance. Constructing the response to historical SST anomalies as a weighted sum of the individual responses is, on the other hand, a simpler problem. Because the historical SSTs are themselves smooth, a simple method where the weights are determined by the patch-average SST value suffices.

Consider the Green's function (more properly a boundary integral) relating seasonal climate anomalies $y(\mathbf{x})$ to anomalous SST boundary conditions $T(\mathbf{x})$ as follows:

$$y(\mathbf{x}) = \int G(\mathbf{x}, \mathbf{x}')T(\mathbf{x}') dA' + \varepsilon(\mathbf{x}), \quad (1)$$

or in discretized form

$$\mathbf{y} = \mathbf{G}\mathbf{T}\delta A + \boldsymbol{\varepsilon}. \quad (2)$$

The vector \mathbf{y} may include all model variables at all model gridpoints or some subset of the entire state vector. Here \mathbf{G} is the matrix form of the Green's function. The residual $\boldsymbol{\varepsilon}$ includes the effects of sampling unpredictable noise as well as deviations from linearity and is in general a function of the SST field (see Sardeshmukh et al. 2000). We will treat $\boldsymbol{\varepsilon}$ as Gaussian random variable that is independent of SST, but this assumption will only be invoked in justifying the optimization properties of the smoothing procedures discussed below. The representative area element, δA , is taken to be constant for this discussion.

The sensitivity $S(\mathbf{x})$ to SST of any scalar function of the model variables $R(y)$ (in our case, area averages of geopotential height and precipitation over specified target regions) is a special case of the Green's function:

$$R = \int S(\mathbf{x}')T(\mathbf{x}') dA' + \varepsilon. \quad (3)$$

In discrete form this is

$$R = \mathbf{s}^T\mathbf{T}\delta A + \varepsilon, \quad (4)$$

where \mathbf{s} is a vector that can be mapped on the same grid as \mathbf{T} , and ε is a scalar. Maps of the sensitivity \mathbf{s} are also known as influence functions. They can be simply derived from the Green's function and represent optimal forcing patterns (Newman and Sardeshmukh 1998).

Some insight into the nature of sensitivity is gained

by examining the units of \mathbf{s} . Note that we have explicitly separated out an area factor in Eqs. (2) and (4) in order to make the matrix Green's function and the sensitivity independent of the size of the area elements in the discretization. This differs from the treatment in Newman and Sardeshmukh (1998) and Grimm and Silva-Dias (1995), who include the area factor in the definition of \mathbf{G} and \mathbf{s} . Separating out the area factor makes it convenient to define a unit that we refer to as the SSTU: 1 SSTU = $10^6 \text{ km}^2 \text{ K}$. The SSTU measures the potential of an extended SST anomaly to force an atmospheric response. For example, a 1-K SST anomaly extending over 10^6 km^2 would have 1 SSTU, as would a 2-K anomaly over half that area. The sensitivity \mathbf{s} is then measured in units of the target R per SSTU.

Applying the Green's function formalism to our array of 42 SST anomaly patches \mathbf{T}_k and the corresponding ensemble mean responses \mathbf{y}_k , we have

$$\mathbf{y}_k = \mathbf{G}\mathbf{T}_k\delta A + \boldsymbol{\varepsilon}_k \quad k = 1, 2, \dots, 42, \quad (5)$$

where we define

$$\mathbf{y}_k = (\mathbf{y}_{k,\text{warm}} - \mathbf{y}_{k,\text{cold}})/2. \quad (6)$$

Given the individual patch responses \mathbf{y}_k we want to do the following. 1) Construct the response to an observed SST field $T(\mathbf{x})$ as a weighted sum of the individual responses:

$$\hat{\mathbf{y}} = \sum_{k=1}^{42} w_k \mathbf{y}_k. \quad (7)$$

2) Estimate the sensitivity of $R(y)$ to SST at some location \mathbf{x} as a weighted sum of the individual responses:

$$\hat{\mathbf{s}}(\mathbf{x}) = \sum_{k=1}^{42} a_k(\mathbf{x})R(\mathbf{y}_k). \quad (8)$$

If the system were truly linear and deterministic then both these tasks could be accomplished by a straightforward least squares projection of $T(\mathbf{x})$ onto the set of \mathbf{T}_k . Because the least squares projection is not orthogonal due to the overlap of the SST patches, it can amplify both the noise and nonlinearity in the residual term of Eq. (1). Instead we will sacrifice some spatial resolution of the sensitivities and seek projections that are smooth in some sense.

For the first task—the response to observed tropical SST fields—we choose the dimensionless weights w_k to be proportional to the weighted average of $T(\mathbf{x})$ over the patch, using the patch function as the weighting function:

$$w_k = \frac{\sum_j T(\mathbf{x}_j)T_k(\mathbf{x}_j)}{3 \sum_j T_k(\mathbf{x}_j)}, \quad (9)$$

where \mathbf{x}_j are the grid points of the GCMs Gaussian grid. We use a constant value of 3 K in the denominator because the sum of all the SST patches corresponds to

a spatially uniform 3 K anomaly over the entire domain, with the exception of the edges. (Recall that the entire grid consists of two rectangular subgrids, each of which adds up to a plateau of 1.5-K amplitude). This procedure is well behaved both because of the uniform spacing of the grid and because the observed SST anomalies tend to be of larger scale than our individual patches. The results of this linear construction are shown in section 4c, and the signal-to-noise ratio of such a construction is discussed in section 4d.

For the second task—estimating sensitivity maps—the issue of sampling becomes critical and the above method falls short. If we compare the forcing potential of a single SST anomaly patch (~ 5 SSTU) to that of a typical ENSO event (say 20–40 SSTU), we can see that signal-to-noise ratio for the remote response to a *single* patch is likely to be small. As a result our estimates of the sensitivity can vary significantly from patch to patch due to sampling. To extract a credible sensitivity map from this noisy data, we define the weights $a_k(\mathbf{x})$ to act as a spatial smoother. Such a spatial smoother combines the results from patches in the neighborhood of \mathbf{x} to increase the effective ensemble size at the expense of spatial resolution of the sensitivity maps. The exact form of the spatial smoother is not critical, though there should be some way of estimating the “correct” degree of smoothing for a given signal-to-noise ratio (SNR) of the target responses. For example, a robust target signal such as the precipitation response directly above the SST anomaly tends to have a high SNR, and thus the raw sensitivities require little smoothing. However, the lower SNR of a midlatitude target may necessitate considerable smoothing to bring out the resolvable sensitivity.

The statistically based “thin-plate smoothing spline” [Wahba 1990; also the RKPACk software package, Gu (1989), available from the Netlib archive], a method from the field of functional data analysis, proved to be a good choice for this problem. In addition to varying the degree of smoothing according to the signal-to-noise ratio for each target, the smoothing spline is easily adapted to our staggered grid and has several other attractive theoretical properties, including transparent relationships to Bayesian estimation and stochastic processes, detailed in Wahba (1990). The smoothing spline for each target is uniquely specified in terms of a single smoothing parameter. This smoothing parameter was chosen so that the resulting mean-square deviation of the raw sensitivities from the smoothed sensitivities is equal to an a priori estimate of the noise variance. We present a more detailed discussion of this method along with examples of raw and smoothed sensitivities in appendix B.

4. Validation of the Green’s function approach

The Green’s function approach is linear. That is, we hypothesize that the seasonal mean signal forced by a

large-scale SST pattern can be approximated by a linear superposition of the responses to our smaller-scale SST patches. Because of the importance of tropical precipitation anomalies in forcing the atmosphere, we will first summarize the precipitation responses to the individual SST anomaly patches. Then we will demonstrate the linearity of the local precipitation response in the Niño-3 and Niño-4 regions using output from a different set of GCM runs. Finally we will assess the extent to which the responses to specified historical SST patterns obtained from Eq. (7) approximate those obtained using the full GCM.

a. Local and global precipitation response

The connection between SST anomalies and tropical precipitation is the first link in the chain leading from SST anomalies to their global teleconnections. The sensitivity of tropical precipitation to SST is determined by a number of factors including the background low-level humidity and wind fields, dynamical (convergence) feedback, changes in evaporation, and possibly by processes included in the parameterization of convection (see appendix A). It is not our intent to present a detailed diagnosis of this sensitivity, but merely to document the connection between SST and convection in this model to aid in the understanding of more distant teleconnections.

First we summarize the spatial structure of the local precipitation response near the SST patches. Figure 2 shows the composite precipitation response for all the SST patches located at latitudes 8.4°N, 0°, and 8.4°S. It consists of a strong positive anomaly located directly over the SST anomaly, accompanied by a weak negative anomaly of nearly the same spatial scale on the equatorward side of the SST anomaly that extends into the opposite hemisphere. In addition there are weaker precipitation anomalies of both signs throughout the Tropics that lie outside the regions shown. The composites for the other four rows of SST patches (not shown) follows a similar progression in structure from north to south. It is tempting to contrast these structures to the idealized solutions of Gill (1980), and indeed there are many differences. It is important to bear in mind that the response to SST forcing is more complicated than the response to Gill’s atmospheric heating. Indeed, the patterns in Fig. 2 would be used as the *forcing* in Gill’s problem.

Second, we define the *local precipitation sensitivity* as the ratio of the area-integrated precipitation anomaly divided by the area-integrated SST anomaly, where the area is that of the SST patch. (Note that this quantity has units of precipitation rate per Kelvin; there is no area factor in the sensitivity because the target itself is an extensive quantity). In Fig. 3a the local precipitation sensitivity ($\times 10$) for each SST patch is plotted at the center point of the patch. Contours are shown every 2 mm day⁻¹ K⁻¹. The strongest

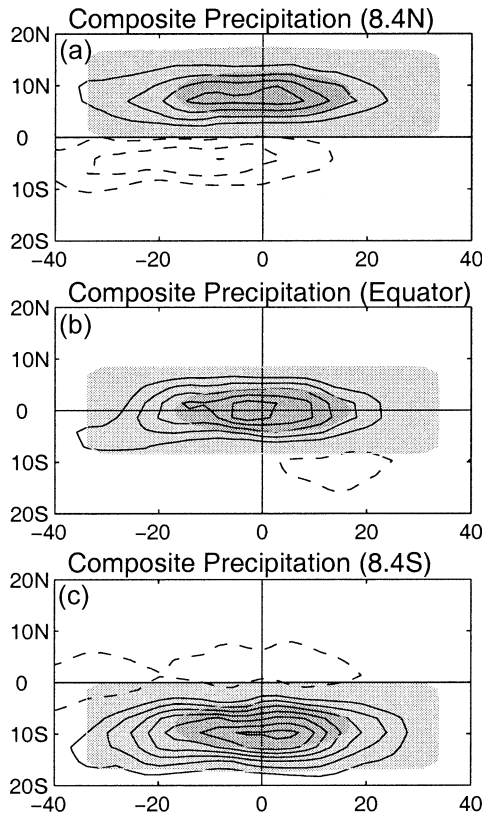


FIG. 2. Composite precipitation response for all SST anomaly patches at (a) 8.4°N , (b) 0° , and (c) 8.4°S lat. The horizontal axis is longitude measured relative to the center of the SST patch. Contour interval is 2 mm day^{-1} . The zero contour is not shown. Shading indicates the area of the SST anomaly patch (light) and the 0.75-K contour (dark).

local response ($5\text{--}9 \text{ mm day}^{-1} \text{ K}^{-1}$) is obtained for SST anomalies south of the equator in a band stretching westward from just east of the date line into the Indian Ocean, including the South Pacific convergence zone (SPCZ). The weakest responses are obtained for SST anomalies in the eastern Pacific.

We can test the linearity of the local precipitation response by computing the equivalent of Fig. 3a for the warm and cold experiments separately, where anomalies are defined relative to the climatological SST runs (not shown). Averaged over the whole domain, the precipitation response in the warm experiments is about 20%–25% stronger than in the cold experiments. Interestingly, much of the warm pool shows a slightly *weaker* local response in the warm cases than in the cold cases. The local precipitation sensitivity maps in the warm and cold cases are correlated with the pattern in Fig. 3a at 0.94 and 0.91, respectively, and are correlated with one another at 0.72. The broad picture—even in the warm pool—is of approximate linearity. The greatest discrepancies occur in the Niño-3 region where the coldest climatological SSTs are located, and for the southern Indian Ocean patches (for which we have no simple explanation).

Finally, we define the *global precipitation sensitivity* by extending the local precipitation and SST integrals to a global domain. These sensitivities are shown in Fig. 3b. Because the SST anomalies are zero outside the patch, the denominator in the definition of global precipitation sensitivity is the same as that for the local precipitation sensitivity. Therefore the local and global sensitivities can be directly compared in terms of total precipitation. For example, their difference provides a measure of the sensitivity of precipitation *outside* the patch to SSTs in the patch. To get the sensitivity of the global precipitation *rate* one needs to multiply the numbers in Fig. 3b by the ratio of the area of the patch to the area of the globe. The largest values of global pre-

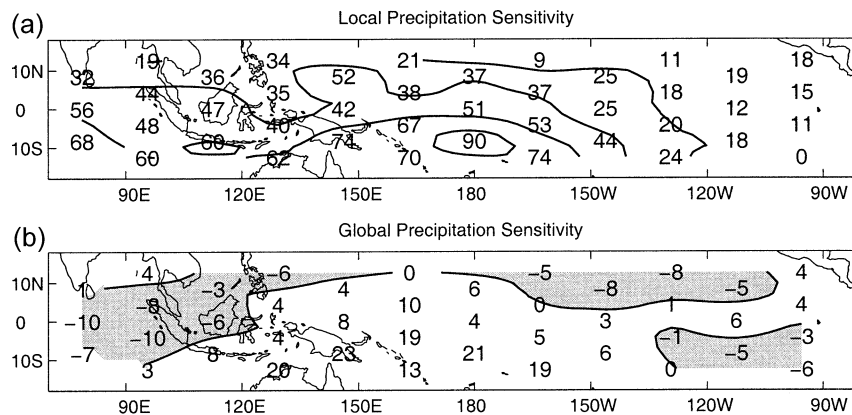


FIG. 3. (a) Local precipitation sensitivity for each SST anomaly patch. The precipitation anomaly (warm – cold) is integrated only over the area of the SST patch and is normalized by the integrated SST anomaly. Units are $0.1 \text{ mm day}^{-1} \text{ K}^{-1}$. Contour interval is $2 \text{ mm day}^{-1} \text{ K}^{-1}$. (b) Global precipitation response, with the same normalization as in (a). Only the zero contour is shown.

precipitation sensitivity are south of the equator between longitudes 130°E and 160°W, where the local precipitation sensitivity is also largest. However it is striking that warm SST anomalies in some regions produce a *negative* global precipitation anomaly (and vice versa). Tropical precipitation sensitivity (not shown), where the area of integration is restricted to latitudes between 30°N and 30°S, is virtually identical to global precipitation sensitivity, indicating that this (over-) compensation of precipitation is a tropical phenomenon.

One unusual feature of this GCM's tropical precipitation is that several different anomaly patches give rise to a precipitation response in the model's SPCZ. The precipitation is apparently important in forcing some Southern Hemisphere circulation anomalies, though we are not certain to what extent this is realistic. Nonetheless we feel that the reader should be aware of this fact when interpreting our sensitivity maps in the Southern Hemisphere.

b. Linearity of Niño-3 and Niño-4 regions

We next consider the linearity of the precipitation response to SST anomalies in the Niño-3 (5°N–5°S, 90°W–150°W) and Niño-4 (5°N–5°S, 150°W–160°E) regions. These are the core regions of interannual tropical SST variability. A separate set of runs was done with the MRF9 GCM prior to the “patch” runs in order to investigate nonlinearity in this region. These runs were done under perpetual January conditions with SST anomalies of –3 K, –1 K, 0 K (climatology), 1 K, and 3 K specified in the Niño-3 region, in the Niño-4 region, and in both regions simultaneously (Niño-3+4). These regions are larger than the SST anomaly patches defined above. An ensemble of 16 runs was generated for each experiment. Figure 4 shows the local ensemble-mean precipitation anomaly in each experiment. In each case the anomaly was defined relative to the ensemble mean of the climatological SST runs. We see that the Niño-3+4 precipitation response (along the diagonal of the figure) is almost exactly the sum of the responses from the Niño-3 and Niño-4 runs separately, strongly supporting the hypothesis of linearity of the local precipitation response. However, the negative SST anomalies lead to a smaller precipitation response than the corresponding positive anomalies, indicating a deviation from true linearity that will be investigated in another paper. Still, a linear (planar) fit to this data captures much of the behavior.

c. Response to historical SST anomalies

A more stringent test of linearity is whether the responses to our set of 42 SST patches can be used to predict how the GCM responds to historical SST patterns. We had at our disposal an ensemble of 12 runs of the MRF9 model performed at NCEP by Ming Ji in which global SSTs were specified to be the 1950–95

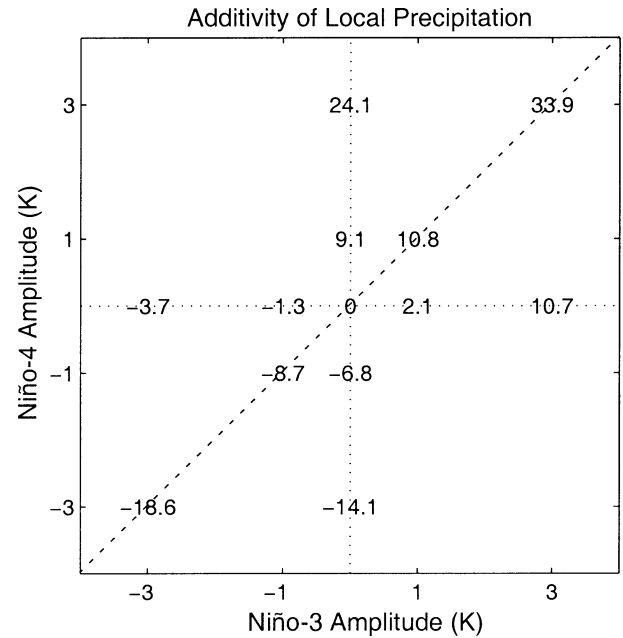


FIG. 4. Local precipitation response for idealized SST anomalies in the Niño-3 region, the Niño-4 region, or in both regions (Niño-3+4) with amplitudes of –3, –1, 1, and 3 K. The numbers on the diagonal correspond to the Niño-3+4 experiments and are almost exactly the sum of the values from the individual Niño-3 and Niño-4 experiments.

observed values. Using the same set of historical SSTs, we combined the individual SST patch responses according to Eqs. (7) and (9). Note that our runs were done in perpetual January conditions while the NCEP runs had a full seasonal cycle, from which we used the DJF average.

To compare the two sets of runs, we examine at each grid point the local correlation coefficient between the ensemble mean of the NCEP runs and the values linearly reconstructed as a weighted average of the responses to our SST patches. Figure 5 shows the correlations for 200-hPa eddy height, spatially filtered to T21 resolution before computing the correlations. The values are high over the entire Tropics, the North Pacific, and in regions of North America that are generally associated with a predictable ENSO signal. In addition, eastern and south-central Asia also exhibit strong correlation, as does a region south of Africa (not shown). In Fig. 6 we show the correlation coefficient for precipitation, spatially filtered as above. The precipitation correlations are greater than 0.8 over much of the central equatorial Pacific, and greater than 0.6 over much of the Tropics, even in locations outside the domain covered by our patches. There are also areas of high correlation over parts of North America, Australia, South Africa, and South America.

Target regions that fail our coarse-grain linearity test (i.e., regions of low correlation in Figs. 5 and 6) may still exhibit interesting sensitivities to tropical SST

200 hPa Height Correlation (T15)

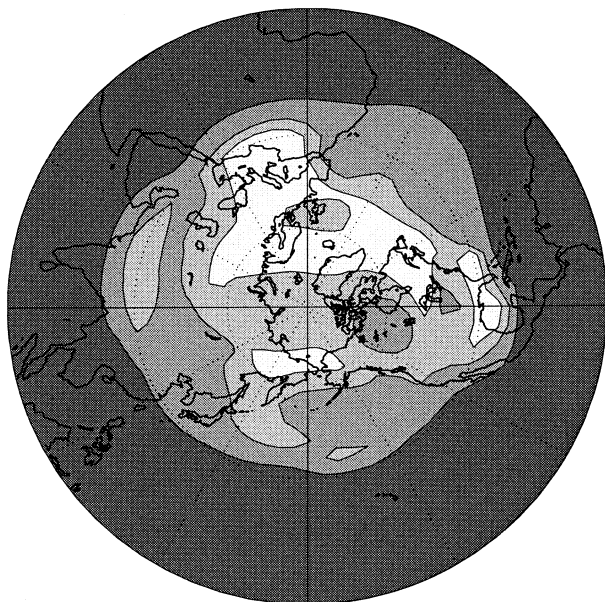


FIG. 5. Correlation of multilinear reconstruction of 200-hPa heights for the period 1950–95 with the DJF mean from a 12-member ensemble of runs with observed SST specified globally. Both fields filtered to T15 spectral truncation. Contour interval is 0.3, with the zero contour suppressed. Shaded areas indicate values greater than 0.3 (light gray), 0.6 (medium gray), and 0.9 (dark gray).

anomalies. For example, consider a target area that exhibits a nonlinear atmospheric response to the dominant ENSO-related SST anomalies in the historical record [see Sardeshmukh et al. (2000) for examples of such areas]. This nonlinear response may mask a linear response to SST anomalies outside the dominant regions of observed SST variability, perhaps located closer to the target area or in regions such as the Indian Ocean. The independence and uniform coverage of our individual patch experiments allow us to determine the atmospheric sensitivity to such non-ENSO related SST anomalies. In addition, a target may fail our linearity test for several reasons besides that of nonlinearity. The signal-to-noise ratio may be small in the target region

when forced by historical SSTs, but may potentially be larger for other SST forcing. The response in the AMIP-style runs may also be sensitive to SSTs that lie outside the domain covered by our patches. Nevertheless, if a target fails our test, sensitivity of that target to SSTs in the Niño-3 and Niño-4 regions should be regarded with some suspicion.

d. Signal-to-noise ratio of the historical SST reconstruction

In this section we discuss the problem of estimating the signal-to-noise ratio (SNR) of the fields we have constructed using historical SSTs. To understand better the trade-off between spatial resolution of the Green's function and SNR, consider the following thought experiment. Suppose that we have an ensemble of runs in which observed tropical SSTs are specified. Assume that we can separate the output of the runs into signal and Gaussian noise as $y = y_s + \mathcal{N}(0, \sigma^2)$. Now suppose that we divide the tropical Pacific domain into two halves, and perform separate GCM runs using only the SST anomalies in each half. If we add the anomalies from the two sets of runs together we can attempt to reconstruct the complete signal. If the signal is perfectly linear and the noise is independent of the signal, then $y_s = y_{s_1} + y_{s_2}$, and $\hat{y} = y_s + \mathcal{N}(0, 2\sigma^2)$. Note that the noise in the reconstructed response is now doubled! To maintain the original SNR we either need to increase the forcing artificially by a factor of $2^{1/2}$ (and hence increase the signal for each subdomain) or double the number of ensemble members.

We can perform a similar analysis on the reconstructed fields defined in Eqs. (7) and (9) for our $M = 8$ member ensembles. Consider for simplicity a scalar variable y . We may write:

$$\hat{y} = \sum w_k y_k \approx \sum w_k y_{s_k} + \sum w_k \mathcal{N}(0, \sigma_{2M}^2),$$

where $\sigma_{2M}^2 = (1/2M)\sigma_0^2$ is the variance of an $2M$ -member ensemble mean of individual runs. [The factor of 2 is a result of the definition of y_k in Eq. (6)]. The reconstructed field then has noise variance equal to

Precipitation Correlation (T15)

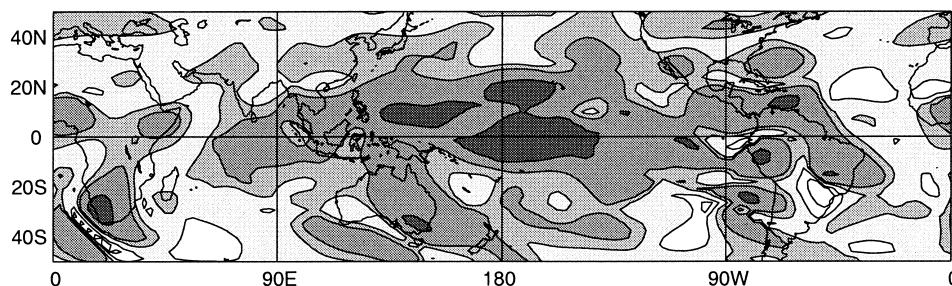


FIG. 6. Correlation between reconstructed (Jan) and historical SST precipitation (DJF). Same contouring as in Fig. 5.

$$\sigma_R^2 = \sigma_{2M}^2 \sum w_k^2 \equiv \frac{\sigma_0^2}{M_{\text{eff}}},$$

where we have introduced the effective ensemble size M_{eff} . Therefore including an SST anomaly patch in the linear reconstruction that has minimal signal may lower the SNR of the entire reconstructed field.

The effective ensemble size for the reconstructed fields may then be expressed as

$$M_{\text{eff}} = 2M \left(\sum w_k^2 \right)^{-1}.$$

For the reconstructions using historical DJF mean SST fields, the mean value for all years of the sum of the squares of the weights w_k is 1.00 (This is an accident! For January SST weights alone the value is 1.17). Therefore the reconstructed field has approximately the same signal-to-noise ratio as a 16-member ensemble with the full SST field specified.¹

5. Sensitivity of global targets

In this section we present sensitivity maps for a selection of targets around the globe. For the most part these targets lie in regions where the linear reconstruction and the historical SST GCM run agree (see Figs. 5 and 6). However, a few targets were chosen in regions where the above test of linearity fails. We believe the sensitivities for these targets are interesting in spite of failing this test, for reasons mentioned in section 4c.

a. 200-hPa heights–PNA pattern

The first target is a variant on the Pacific–North American circulation pattern that is a characteristic pattern of Northern Hemisphere variability. We define the PNA pattern in terms of the standardized 200-hPa eddy heights in the 10° lat \times 20° lon region surrounding the “centers of action” of the classic PNA pattern (Wallace and Gutzler 1981). The smoothed SST-forcing sensitivity map for the PNA index is shown in Fig. 7a. The “+” and “–” symbols in the figure depict the signs of the regionally averaged height anomalies that go into computing the index. In general, warm SST anomalies in the tropical Pacific result in positive PNA values. The greatest sensitivity is to SST anomalies located in and south of Niño-4. There is a nodal line in the sensitivity at about 100° E longitude, with warm SST anomalies in the Indian Ocean resulting in a negative value of the PNA index. These results are consistent in their general structure to the results of Ting and Sardeshmukh (1993). Using a linear baroclinic model forced by localized heating anomalies, they found a PNA-like response that is

in the same sense as ours with a node in the sensitivity at 120° E longitude. Newman and Sardeshmukh (1998) show barotropic sensitivity maps for a variant of the PNA pattern that excludes the center near Hawaii. Their PNA pattern shows wintertime sensitivity to positive Rossby wave forcing in a swath stretching across the central Pacific on the equatorward side of the jet that is usually associated with diabatic forcing farther south (Sardeshmukh and Hoskins 1988). There is also a swath of sensitivity to negative Rossby wave forcing over the western Pacific at about 10° N latitude. It is plausible that a Rossby wave source could be generated in these swaths by an SST anomaly having the same pattern as the sensitivity map shown in Fig. 7a. Therefore the patterns of sensitivity to Rossby wave forcing in Newman and Sardeshmukh (1998) are roughly consistent with our SST sensitivity patterns.

In Fig. 7b we show the sensitivity of the anticyclonic center of the PNA pattern over western Canada. Here again, the Niño-4 region dominates the sensitivity. Positive sensitivities (i.e., when warm SST anomalies correspond to high geopotential heights over the target region) extend throughout most of entire domain. This figure is included to demonstrate that the sensitivity of the PNA pattern to Niño-4 in Fig. 7a is not solely due to the sensitivity of the nearby height response over the North Pacific Ocean.

The observed variability of the PNA pattern depends on both the sensitivity of SST forcing and on the variability of the SST itself. To get a sense of the locations where historical SST anomalies would have a strong influence on the PNA pattern in this model, we show the product of the PNA sensitivity with the standard deviation of observed January mean SSTs for the period 1950–95 in Fig. 7c. Compared to the PNA sensitivity (Fig. 7a) the pattern is more focused near the equator and shifted toward the Niño-3.4 region (5° N– 5° S, 120° – 170° W). However, the maximum does not lie as far east as the maximum in SST variability (Fig. 1b). It should be borne in mind, however, that Fig. 7c shows only the local contribution of SSTs to the variability of the PNA pattern.

b. Precipitation targets in North America

Figure 8 shows five precipitation target regions of interest over North America. These were chosen as regions of coherent variability from examination of one-point correlation maps as described in appendix B, and thus indicate regions over which smaller targets would produce similar sensitivity maps. For target A in the southeastern United States we see a similar sensitivity pattern to the 200-hPa heights, with a dominance by the Niño-4 region. The positive sensitivities extend in a broad swath from Indonesia to Central America. Warm SST anomalies in these areas force a wet anomaly in the target region. There is a large region of negative sensitivity west of the Philippines. Target B over the

¹ Note, however, that this rough equivalence applies only to the analysis of the *reconstructed* response to historical SSTs. The wealth of sensitivity information in our 42-patch dataset is considerably greater than in 16-member AMIP ensembles, especially in regions of small historical SST variability.

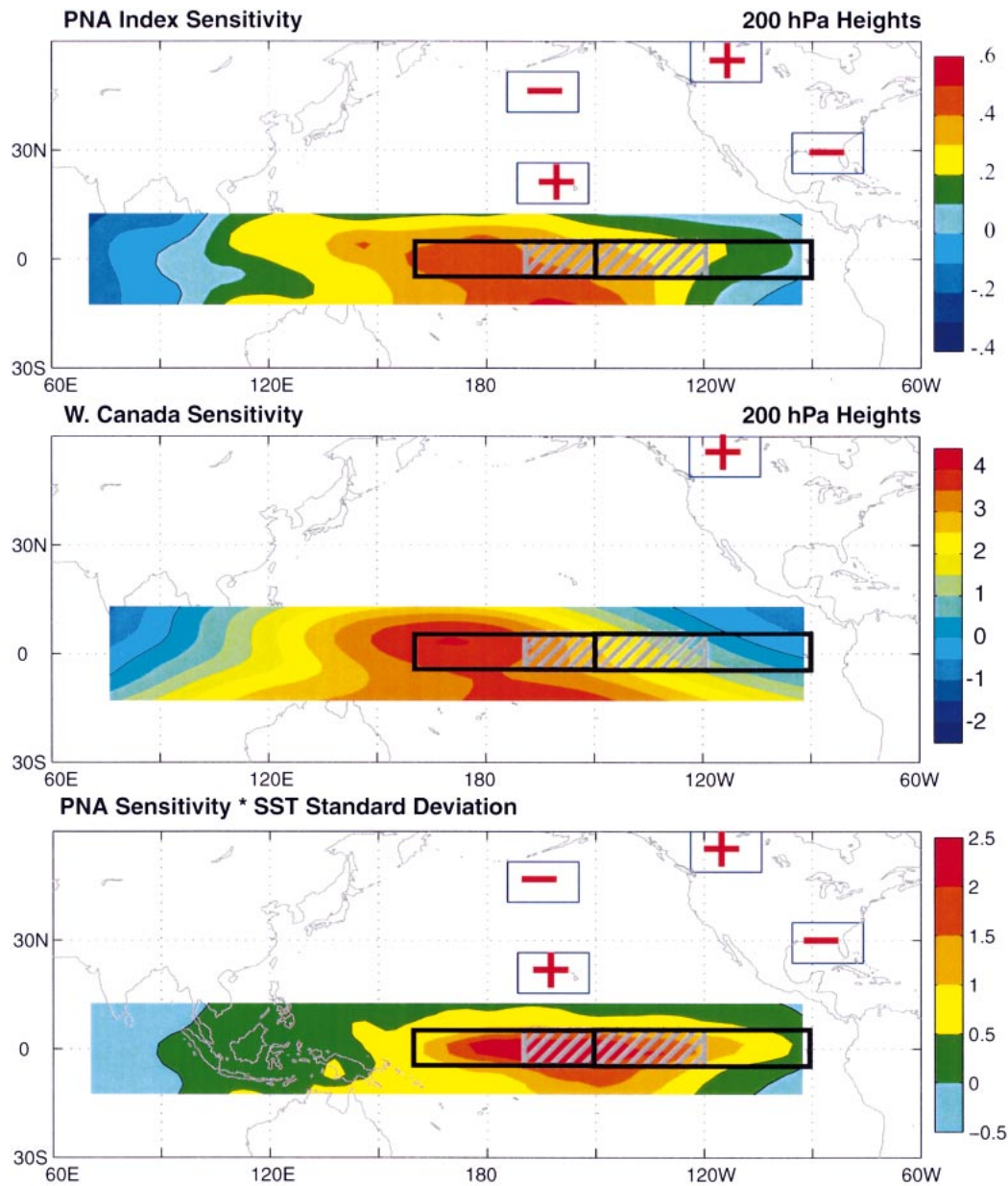


FIG. 7. (a) Sensitivity of the PNA index defined from 200-mb heights (contour interval is 0.1 SSTU^{-1}). Target regions that were used to define the PNA pattern and the signs of their contributions to the index are indicated. The Niño-4 and Niño-3 regions are depicted by black rectangles on the equator; the Niño-3.4 region by a gray hatched rectangle. (b) Sensitivity of the center over western Canada (0.5 m SSTU^{-1}). (c) PNA sensitivity multiplied by the standard deviation of Jan SSTs ($0.5 \times 10^{-6} \text{ km}^{-2}$). SSTs have been interpolated through land points.

southwestern United States and northwestern Mexico is located in a climatologically dry region. It too shows a region of positive sensitivity stretching from the Niño-4 region through Indonesia. In contrast to target A, the map for target B has a region of negative sensitivity to SST anomalies off the coast of Central America. Proceeding to target C over the northwestern United States, we see an interesting pattern with weak negative sensitivities at the dateline surrounded by regions of strong positive sensitivity in and north of Niño-3 and west of

the Philippines. Target D over the central United States is not usually identified as a region that is sensitive to El Niño, and indeed this study confirms that. However, there is an intriguing sensitivity to SST anomalies in Indonesia (which represent results from more than one patch), which bears further investigation. Finally, the sensitivities for precipitation over the northeastern United States appear to be small or nonexistent, with the possible exception of sensitivity to SSTs near South America.

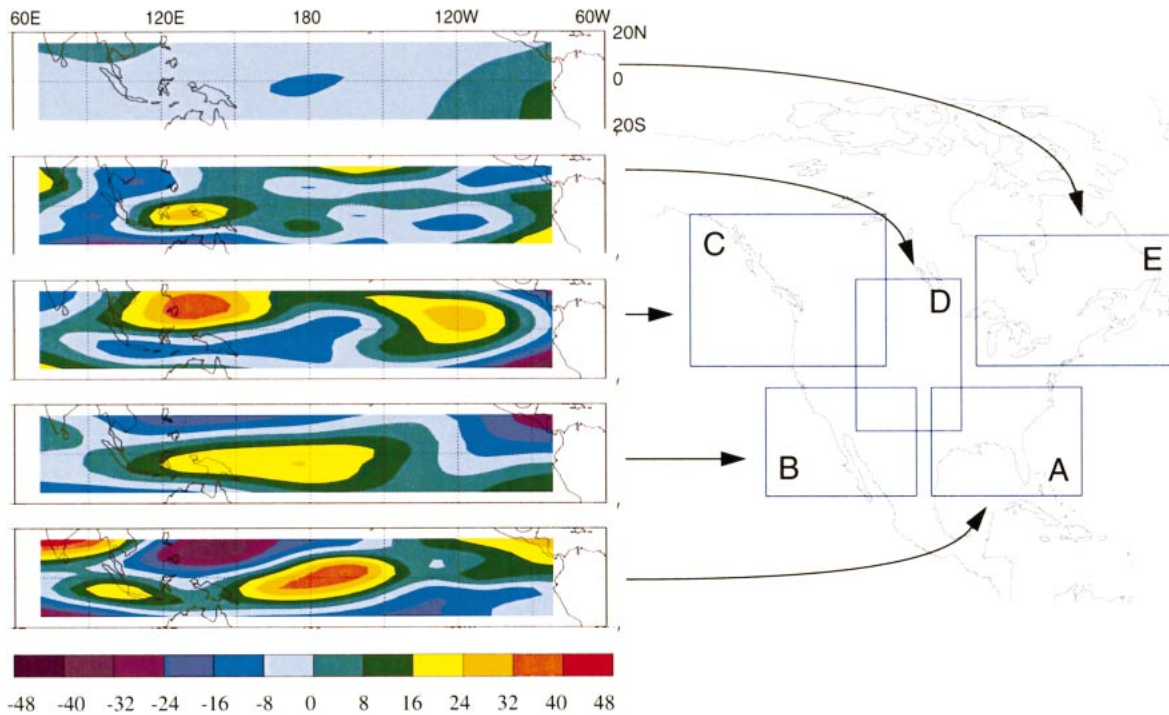


FIG. 8. Precipitation sensitivity for five regions in North America. Contour interval is $8 \times 10^{-3} \text{ mm day}^{-1} \text{ SSTU}^{-1}$. For example, a sensitivity of 20 in these units means that a 1-K SST anomaly with an areal extent of 10^8 km^2 would result in 0.2 mm day^{-1} increased precipitation in the target area.

c. Precipitation targets in South America, Africa, Australia, Indonesia

Precipitation sensitivities for three target areas in South America are shown in Fig. 9. These targets were also chosen through the use of one-point correlation maps. They are the three primary South American regions where the SST anomaly patches had a large effect in modulating the seasonal mean precipitation. In these target areas the linear reconstruction also corresponds well to the NCEP global SST runs (see Fig. 6). These maps indicate that South American precipitation is most sensitive to SST anomalies in the central tropical Pacific,

with opposite sensitivities for precipitation in northeastern Brazil and the Peru–Ecuador region. Physically this is consistent with convection in the central Pacific forcing a large-scale circulation pattern of which the precipitation responses are the local expressions.

For Africa we have chosen three precipitation targets, shown in Fig. 10. The targets in the horn of Africa and in southwestern Africa are regions where our linear reconstructions agree well with the historical SST runs. This is not the case for the Madagascar target [see also Fig. 6 of Sardeshmukh et al. (2000), who detect a non-linear ENSO signal over Madagascar], but we include

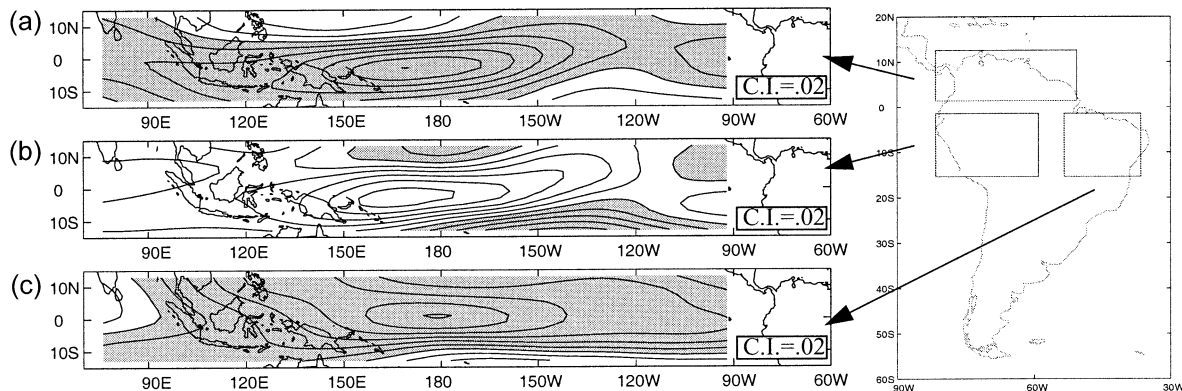


FIG. 9. Precipitation sensitivity for (a) northern South America, (b) Peru/Ecuador, and (c) northeastern Brazil. Contour interval is $0.02 \text{ mm day}^{-1} \text{ SSTU}^{-1}$. Negative values are shaded.

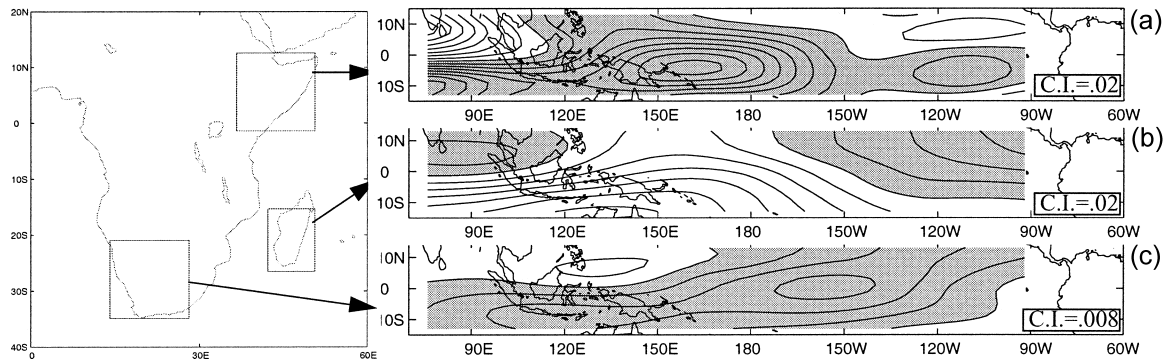


FIG. 10. Precipitation sensitivity for (a) East Africa, (b) Madagascar, and (c) southwestern Africa. Contour interval is $0.008 \text{ mm day}^{-1} \text{ SSTU}^{-1}$ for southwestern Africa, 0.02 for the others. Negative values are shaded.

it because there is a strong signal in that region that shows interesting sensitivity in the Indian Ocean. For all three targets there are sensitivities to SST anomalies in the western and central equatorial Pacific in addition to a north–south dipole of sensitivity to Indian Ocean SST anomalies. In fact, for southern Africa, the strongest sensitivities lie to the east of the date line. Goddard and Graham (1999) discuss the “dominant influence” of Indian Ocean SST anomalies in forcing the main pattern of African rainfall variability in the ECHAM GCM. Our study suggests a more complicated picture, particularly in regard to SST anomalies in the western Pacific and Maritime Continent, that would not be detected in their analysis because of their reliance on the dominant patterns of historical SST variability. Interestingly, their study also shows a strong relationship between the canonical ENSO SST anomalies in the Pacific Ocean and rainfall in southern Africa, consistent with our sensitivities.

Australia exhibits two coherent regions of sensitivity according to the one-point correlation maps. Sensitivities to these targets are shown in Fig. 11. The southeastern Australia target also is an area where our linear reconstructions and the historical SST runs coincide. In January, Australia is most sensitive to SST anomalies to the north of the continent with warm water there

leading to more precipitation in the target regions. For southeastern Australia precipitation there is a region south of the equator between longitude 120°W and the date line where the sensitivities are in the opposite sense.

Precipitation sensitivity in the vicinity of Indonesia is also shown in Fig. 11. Understanding drought that occurs in this area during El Niño conditions is an important problem. January is in the wet season in Indonesia. In this study there is a large local sensitivity to SST anomalies, with warm water leading to increased precipitation locally, and cold water leading to decreased precipitation. Opposite sensitivity prevails outside the immediate vicinity of the target, with the maximum sensitivity located north of the equator at 150°E longitude. Given the typical observed patterns of SST variability, there is likely to be a delicate interplay of the local and remote SST effects in determining the rainfall of this region. Haylock and McBride (2001) argue that DJF Indonesian rainfall is “inherently unpredictable” based on the lack of spatial coherence of rainfall anomalies. Perhaps the lack of spatial coherence is due to the complicated relationship between SST and rainfall that we have shown in this model. In fact, it is unclear to the authors whether—or more accurately, on what timescale—SST anomalies in the vicinity of the Maritime Continent can be considered as “forcing,”

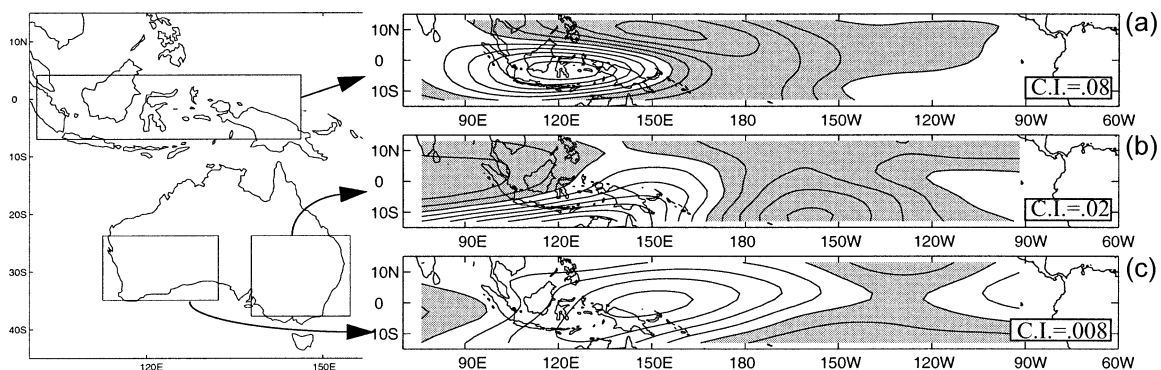


FIG. 11. Precipitation sensitivity for (a) Indonesia (contour interval is $0.08 \text{ mm day}^{-1} \text{ SSTU}^{-1}$), (b) southeastern Australia (contour interval is $0.02 \text{ mm day}^{-1} \text{ SSTU}^{-1}$), (c) southwestern Australia (contour interval is $0.008 \text{ mm day}^{-1} \text{ SSTU}^{-1}$). Negative values are shaded.

because of the strong local feedback between precipitation and SST in that region. Perhaps there is still hope for successful prediction of wet season precipitation in this region, but one needs to look beyond a single ENSO SST pattern or index as a predictor.

6. Conclusions

We have computed the sensitivity of the global atmosphere on seasonal and longer timescales to localized SST anomalies in the tropical Indian and Pacific Oceans. The sensitivity maps for global circulation targets reveal interesting structure. The PNA pattern and 200-hPa geopotential heights over western Canada are most sensitive to SST anomalies in the Niño-4 region of the central equatorial Pacific. We find a nodal line near 100°E longitude in the sensitivity of the PNA to SST forcing, reproducing in this GCM the results of earlier theoretical studies. Niño-4 also dominates the sensitivities for precipitation over the southeastern United States and for some important South American target regions. Precipitation for the African, Australian, and Indonesian targets tend to have their largest sensitivity located to the west of the date line, though most of these had considerable sensitivity to SSTs east of the date line as well.

The overall importance of the Niño-4 region as a locus of strong SST sensitivity has important implications. Recently much attention has been paid to SST anomalies in the Niño-3.4 region, which lies to the east of Niño-4. Based on empirical studies it is currently believed that Niño-3.4 SSTs provide the single best local SST predictor of seasonal climate anomalies over North America. As such the skill in predicting the Niño-3.4 index is a commonly used metric of SST forecast models. In our study, however, Niño-3.4 is not a coherent region in terms of climate sensitivities. Sensitivities vary greatly over the Niño-3.4 region, sometimes even changing sign. On the other hand, Niño-4 appears to be a more coherent region of sensitivity.

Note that the *observed* climate variability depends on both the amplitude of the anomalous SST forcing and on the sensitivity to that forcing. Our study indicates that the observed SST-forced variability over the PNA region is likely the product of the generally increasing SST anomaly amplitudes *and* the generally decreasing sensitivities as one moves east from the date line (Fig. 7c). The large sensitivities of many targets to SSTs *at and west of the date line* indicates a need to predict the tropical SST field accurately in that region. But sensitivity can be a double-edged sword. It is important to recognize that both the predictable SST signal and unpredictable SST noise (or forecast error) can be propagated globally by the Green's function. The same rms forecast error in SST will typically have a larger remote impact in this GCM if it is located in Niño-4 than if it is located in Niño-3.4.

We have taken care to justify the robustness and meaningfulness of the sensitivity patterns we have

shown. First, we have made a plausible case that the coarse-grain linear part of the response to SST anomalies is captured by our method. This linear part seems to comprise a surprisingly large portion of the total response to historical SST anomalies. Second, we have carefully addressed statistical sampling issues. We believe that our sensitivity patterns are robust (at least in the context of this model) because of the properties of the statistically based smoothing we have used. Unfortunately it is difficult, if not impossible, to extract geographically localized sensitivities of the kind shown here from observational analyses or from AMIP-style GCM runs with historical SST forcing during the past half-century. Several factors conspire to bring this about: the relatively short observational record, the high spatial correlation of SST anomalies, and the modest signal-to-noise ratios of remote responses.

We cannot discount the possibility that the dominance of Niño-4 as a sensitive forcing region is a peculiarity of this GCM. However the large sensitivities there certainly warrant a closer look at this important region. The usual warnings about the accuracy of GCM results apply, and these warnings are even more relevant in the case of the perpetual January situation presented here. Further work with this and other GCMs will help establish these sensitivities with greater robustness throughout the seasonal cycle.

In closing, it is worth stressing that our results are equally relevant for assessing atmospheric sensitivity to changes in tropical SSTs on decadal to centennial scales associated with natural as well as anthropogenic forcing. In this context, perhaps the most surprising sensitivity we find is for globally integrated precipitation. For over one-third of the tropical domain considered here, the sensitivity is such that warm SST anomalies act to *reduce* global mean precipitation. Therefore changes in the intensity of the hydrological cycle may depend sensitively on the projected pattern of regional tropical SST changes in global change scenarios. A particularly important region in this regard may be the west Pacific/east Indian Ocean warm pool.

Acknowledgments. Members of NCEP's coupled modeling branch were especially helpful in providing the GCM used in this study. Sara Zhang's assistance is also gratefully acknowledged. The comments of the reviewers and of John Bergman were much appreciated. This research was partly supported by a grant from NOAA's Office of Global Programs.

APPENDIX A

NCEP MRF9

The NCEP MRF9 general circulation model is run at a horizontal spectral resolution of T40 with 18 sigma-coordinate vertical levels. Some features of this model are: a Kuo-type convection scheme, diagnosed clouds

(using a modified Slingo scheme), and a modified Penman–Monteith evapotranspiration scheme with a simple three-layer soil moisture and temperature model. Complete radiative transfer calculations in the free atmosphere are performed every 12 h, though an approximation of the diurnal cycle is included.

One detail of the convection scheme deserves some discussion for its potential effect on the local precipitation sensitivity (Fig. 3a). For convection to occur at ocean grid points in this GCM, moisture convergence (including evaporation) at low levels is required to be greater than a threshold value. This threshold has an explicit dependence on SST, going from its full value at 25°C to zero at 31°C, with strong inhibition of convection below 26.5°C and little inhibition above 28.5°C. This quasi-empirical threshold represents a physical process—the stabilization of the boundary layer above cold SSTs. However, this threshold is only important away from regions of strong mean convergence. Since the largest sensitivities in Fig. 3a tend to occur in regions of copious mean precipitation, other processes must also play a role, including differences in the background humidity field, changes in evaporation, and dynamical (convergence) feedback.

The model was run in perpetual January conditions. The solar declination was fixed at 15 January values. Snow cover, soil moisture, surface roughness over the ocean, and the upper two levels of soil temperature were allowed to evolve. Sea ice, surface roughness over land, the reference land surface albedo, and plant resistance were fixed at mean January conditions. Deep soil temperature was fixed to annual mean conditions.

We first performed a 70-month control run with climatological January SST boundary conditions. The ensemble of initial conditions were chosen from among the daily output restart files (sampled every 5 days) of the 70-month control run. A criterion based on the projection of the daily output onto the first two EOFs of Northern Hemisphere 500-mb height was used to select the initial conditions. In addition, the initial conditions were chosen so that the ensuing 4-month runs had minimal overlap. This particular choice of initial conditions was done with the intention of studying the influence of initial conditions on forecast skill in a separate study. The details of this method will not be presented here. Because the ensemble mean and variance of the ensemble of initial conditions were not biased by our procedure, we do not believe we have introduced a bias in the seasonal-mean statistics shown in this paper.

APPENDIX B

Smoothed Sensitivity Maps

a. Smoothing splines

The statistically based “thin-plate smoothing spline” [Wahba 1990; also the RKPACK software package, Gu

(1989), available from the Netlib archive] proved to be a good choice for our problem. In the smoothing spline formalism one fits a continuous smooth function to the data points by minimizing the mean square error of the smooth function at the data points, subject to a penalty function based on spatial derivatives of the smooth function. The problem is actually solved using an equivalent formulation in which the data are projected onto a Hilbert space of smooth functions. In our case, we chose a “thin-plate” penalty function that penalizes only second derivatives. As the name thin-plate suggests, this particular penalty function is appropriate for Euclidean geometry, not for the sphere. However the domain of our SST patches is restricted to the deep Tropics so their geometry is approximately Euclidean.

There is only one smoothing parameter, λ , which was chosen to be independent of the tropical spatial coordinate \mathbf{x} . It was chosen so that the resulting mean-square deviation of the data points (i.e., raw sensitivities) from the smooth function (i.e., smoothed sensitivities) is equal to an a priori estimate of the noise variance ε^2 in Eq. (4) under the assumption that the noise is independent and Gaussian of uniform amplitude.² If no such λ exists, the best linear fit to the data is used (which contains no second derivatives and hence lies in the null space of the thin-plate penalty function). The noise variance was estimated by computing the variance of the $R(\mathbf{y}_k)$ defined for the individual ensemble members, about the ensemble mean value of $R(\mathbf{y}_k)$ and then pooling the variance for all the patches. The resulting variance of individual ensemble members was divided by the ensemble size ($M = 8$) in order to get our pooled estimate of the noise variance for the ensemble means themselves. Our SST perturbations are sufficiently small that we expect the level of noise in the remote response to be roughly independent of the location of the tropical SST anomaly. Finally, we set the thin-plate penalty function to be anisotropic so that the smoothing length scale is four times greater in the zonal direction than in the meridional direction, consistent with the aspect ratio and spacing of our SST anomaly patches.

b. Raw versus smooth sensitivity maps

What follows is a step-by-step illustration of how we construct most of the sensitivity maps shown in this paper. For the first example we choose precipitation as our target variable. We then select a target point and examine the one-point correlation map among the ensemble mean responses (Fig. B1a). Using the one-point correlation map as a guide, we select a target region

² As an alternative method we attempted to use the generalized cross validation (GCV) algorithm of Wahba (1990) to determine λ . However this method often failed to converge to anything close to a reasonable result compared to our a priori estimates. This failure is understandable because the success of GCV is dependent on sampling at a large number of points (Wahba 1990).

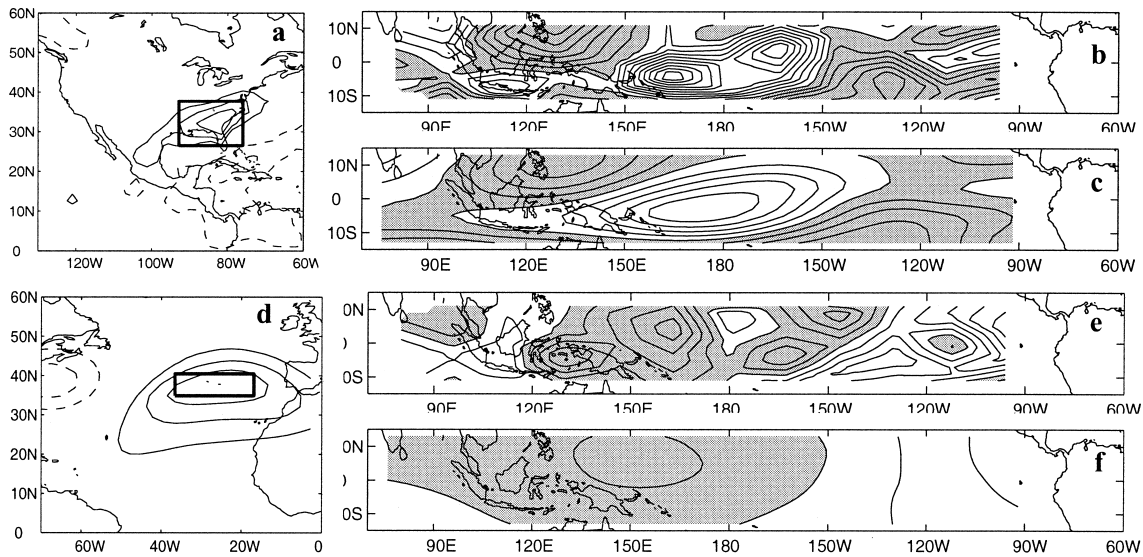


FIG. B1. Raw and smoothed sensitivity maps. (a) One-point correlation map of ensemble mean precipitation. Contours of +0.4, +0.6, and +0.8 are shown. (b) Raw sensitivities (contour interval is $8 \times 10^{-3} \text{ mm day}^{-1} \text{ SSTU}^{-1}$). (c) Smoothed sensitivities. (d)–(f) Same as (a)–(c) except for 200-hPa eddy height (zonal mean removed) sensitivities for target over the Azores. Contour interval in (e)–(f) is 0.4 m SSTU^{-1} . Negative values are shaded.

over which to average precipitation, avoiding target regions with large cancellations within them. The precipitation target regions discussed in the main text are listed in Table B1.

Once the target is selected, we examine the raw sensitivity map. The raw sensitivity map is constructed by plotting the values of the target $R(\mathbf{y}_k)$ for each SST patch at \mathbf{x}_k , the central coordinates of the patch. The resulting staggered array of values is then contoured (Fig. B1b). Clearly there is a lot of noise in the raw estimate of the

sensitivity. To extract a signal from this noisy data, we apply the thin-plate smoothing spline to the raw estimates. The resulting smoothed sensitivity is shown in Fig. B1c. The variance of the raw data about the smoothed estimate is equal to our a priori estimate of the noise variance in the target region derived from the pooled individual ensemble members. Smoothing has removed some of the local maxima and minima, but most of the large-scale structure of the sensitivity is retained.

Another example of the effects of applying the smoothing spline is shown in Figs. B1d–f. Here the target is 200-hPa eddy heights over the Azores. In this case, the smoothed map shows a relatively bland structure of sensitivity compared to the raw sensitivities. Therefore, most of the spatial variation we see in the raw sensitivity map is consistent with the level of noise determined from the individual GCM runs. In some even more extreme cases where the signal is very small, no smoothed structure can be identified. In that case, the smoothing spline returns a result that lies in the null space of the smoothing penalty function—in our case a linear fit to the raw data.

TABLE B1. Precipitation target areas. Latitude and longitude are measured as positive north and east, respectively.

Location	Center		Dimensions	
	Lat (°)	Lon (°)	Lat (°)	Lon (°)
N. America				
Northwestern	50.2	−125.2	19.5	36.6
Southwestern	30.7	−115.3	14.0	28.1
Northeastern	48.8	−71.7	16.7	36.6
Southeastern	30.7	−84.4	14.0	28.1
Central	41.9	−102.7	19.5	19.7
S. America				
Northern	7.0	−66.1	11.2	30.9
Peru/Equador	−8.4	−70.3	14.0	22.5
Northeast Brazil	−8.4	−45.0	14.0	16.9
Africa				
Horn of Africa	5.6	43.6	14.0	14.1
Southwest	−27.9	21.1	14.0	14.1
Madagascar	−20.9	46.4	11.2	8.4
Australia/Indonesia				
Southeastern	−30.7	146.2	14.0	16.9
Southwestern	−29.3	122.3	11.2	19.7
Indonesia	0.0	−119.5	8.4	30.9

REFERENCES

- Barsugli, J. J., P. D. Sardeshmukh, and S. Zhang, 1997: Identifying the most sensitive areas of tropical SST forcing for midlatitude seasonal prediction. *Proc. Seventh Conf. on Climate Variations*, Long Beach, CA, Amer. Meteor. Soc., 166–167.
- Branstator, G., 1985: Analysis of general circulation model sea-surface temperature anomaly simulations using a linear model. Part I: Forced solutions. *J. Atmos. Sci.*, **42**, 2225–2241.
- Chen, W. Y., and H. M. Van den Dool, 1997: Atmospheric predictability of seasonal, annual, and decadal climate means and the

- role of the ENSO cycle: A model study. *J. Climate*, **10**, 1236–1254.
- Ferranti, L., F. Molteni, and T. N. Palmer, 1994: Impact of localized tropical and extratropical SST anomalies in ensembles of seasonal GCM integrations. *Quart. J. Roy. Meteor. Soc.*, **120**, 1613–1645.
- Geisler, J. E., M. L. Blackmon, G. T. Bates, and S. Muñoz, 1985: Sensitivity of January climate response to the magnitude and position of equatorial Pacific sea surface temperature anomalies. *J. Atmos. Sci.*, **42**, 1037–1049.
- Gill, A. E., 1980: Some simple solutions for heat-induced tropical circulation. *Quart. J. Roy. Meteor. Soc.*, **106**, 447–462.
- Goddard, L., and N. E. Graham, 1999: Importance of the Indian Ocean for simulating rainfall anomalies over eastern and southern Africa. *J. Geophys. Res.*, **104**, 19 099–19 116.
- Gu, C., 1989: RKPACK and its applications: Fitting smoothing spline models. *Proceedings of the Statistical Computing Section*, American Statistical Association, 42–51.
- Haylock, M., and J. McBride, 2001: Spatial coherence and predictability of Indonesian wet season rainfall. *J. Climate*, **14**, 3882–3887.
- Kumar, A., M. Hoerling, M. Ji, A. Leetmaa, and P. Sardeshmukh, 1996: Assessing a GCM's suitability for making seasonal predictions. *J. Climate*, **9**, 115–129.
- Livezey, R. E., M. Masutani, A. Leetmaa, H. Rui, M. Ji, and A. Kumar, 1997: Teleconnective response of the Pacific–North American region atmosphere to large central equatorial Pacific SST anomalies. *J. Climate*, **10**, 1787–1820.
- Newman, M., and P. D. Sardeshmukh, 1998: The impact of the annual cycle on the North Pacific/North American response to remote low-frequency forcing. *J. Atmos. Sci.*, **55**, 1336–1353.
- Palmer, T. N., and D. A. Mansfield, 1984: Response of two atmospheric general circulation models to sea-surface temperature anomalies in the tropical east and west Pacific. *Nature*, **310**, 483–485.
- Peng, P., A. Kumar, A. G. Barnston, and L. Goddard, 2000: Simulation skills of the SST-forced global climate variability of the NCEP-MRF9 and the Scripps-MPI ECHAM3 models. *J. Climate*, **13**, 3657–3679.
- Sardeshmukh, P. D., and B. J. Hoskins, 1988: The generation of global rotational flow by steady idealized tropical divergence. *J. Atmos. Sci.*, **45**, 1228–1251.
- , G. P. Compo, and C. Penland, 2000: Changes of probability associated with El Niño. *J. Climate*, **13**, 4268–4286.
- Simmons, A. J., 1982: The forcing of stationary wave motion by tropical diabatic heating. *Quart. J. Roy. Meteor. Soc.*, **108**, 503–534.
- , J. M. Wallace, and G. W. Branstator, 1983: Barotropic wave propagation and instability, and atmospheric teleconnection patterns. *J. Atmos. Sci.*, **40**, 1363–1392.
- Smith, T. M., R. W. Reynolds, R. E. Livezey, and D. C. Stokes, 1996: Reconstruction of historical sea surface temperatures using empirical orthogonal functions. *J. Climate*, **9**, 1403–1420.
- Ting, M., and P. D. Sardeshmukh, 1993: Factors determining the extratropical response to equatorial diabatic heating anomalies. *J. Atmos. Sci.*, **50**, 907–918.
- Wahba, G., 1990: *Spline Models for Observational Data*. CBMS-NSF Regional Conference Series in Applied Mathematics, Vol. 59, Society of Industrial and Applied Mathematics, 169 pp.
- Wallace, J. M., and D. S. Gutzler, 1981: Teleconnections in the geopotential height field during the Northern Hemisphere winter. *Mon. Wea. Rev.*, **109**, 784–812.